Revista Mexicana de Astronomía y Astrofísica, **46**, 363–373 (2010)

THE ABSOLUTE PARAMETERS FOR NSVS 11868841[1] AND THE OVERSIZED STARS IN LOW-MASS ECLIPSING BINARIES

Ö. Çakırlı,[2,3] C. İbanoğlu,[2] and A. Dervişoğlu[2]

Received 2010 April 12; accepted 2010 July 29

RESUMEN

Se han realizado observaciones espectroscópicas de la binaria eclipsante de baja masa NSV 11868841, y se han derivado las velocidades radiales de ambas componentes. Las masas y radios dererminados son $M_1 = 0.870 \pm 0.074\ M_\odot$, $M_2 = 0.607 \pm 0.053\ M_\odot$, $R_1 = 0.983 \pm 0.030\ R_\odot$, $R_2 = 0.901 \pm 0.026\ R_\odot$. Los radios de ambas componentes son, respectivamente, 10% y 57% mayores que los que corresponden a estrellas de la secuencia principal de edad cero y de las mismas masas. Esta discrepancia puede deberse a que ambas estrellas tienen una gran cobertura por manchas. Hemos reunido parámetros absolutos para 21 binarias eclipsantes de doble línea y de baja masa, para comparar sus posiciones en los diagramas masa-radio y masa-temperatura efectiva. Los valores altos de los radios y las bajas temperaturas efectivas encontradas no son debidos a diferencias en metalicidad o en longitud de mezcla. Las discrepancias encontradas para estrellas de baja masa pueden deberse a campos magnéticos que inhiben el transporte convectivo, lo cual propicia una gran cobertura de la superficie estelar por manchas magnéticas.

ABSTRACT

Spectroscopic observations of the low-mass eclipsing binary NSVS 11868841 have been obtained and the radial velocities were derived for both components. The masses and radii determined for the components are $M_1 = 0.870 \pm 0.074\ M_\odot$, $M_2 = 0.607 \pm 0.053\ M_\odot$ and $R_1 = 0.983 \pm 0.030\ R_\odot$, $R_2 = 0.901 \pm 0.026\ R_\odot$. Both the primary and secondary stars' radii are 10% and 57% larger than those of zero-age-main-sequence stars with the same masses. This discrepancy may arise from the large spot coverage of both stars. We collected absolute parameters of 21 low mass double-lined eclipsing binaries and compared their positions in the mass-radius and mass-effective temperature panels. The large radii and lower effective temperatures found for NSV 11868841 are solved neither with differences in metallicity nor in mixing length parameters. These discrepancies for low mass stars may be due to magnetic fields inhibiting the convective energy transport, which lead to a large magnetic spot coverage of the surface of such low mass stars.

Key Words: binaries: eclipsing — stars: activity — stars: fundamental parameters — stars: low-mass

1. INTRODUCTION

Eclipsing binaries are the best laboratories for determining the fundamental physical properties of stars. Detached, double-lined eclipsing binaries yield direct and accurate measures of the masses and radii of the component stars. Measuring these quantities has always been observationally challenging. Large-scale surveys, providing imaging and photometric catalogues for substantial fractions of the celestial sphere, are now available at a wide range of wavelengths. Over the last few years, these surveys have become invaluable research tools for investigating the properties of intrinsically rare objects. These surveys have proven most useful in searches for low-mass stars. Stars with masses less than 1 $M_\odot$ are regarded as low-mass stars and have late spectral types, namely G, K or M. We cannot vary the con-

[1]Based on spectroscopic observations collected at TÜBİTAK National Observatory, Turkey.

[2]Ege University, Science Faculty, İzmir, Turkey.

[3]Tübitak National Observatory, Akdeniz University Campus, Turkey.

ditions prevalent on an individual star, but observations of many individual stars can be combined to build up a picture of how stars of different mass and composition evolve. Since the intermediate- and high-mass stars are intrinsically bright sources, most studies have centered on them, with little consideration of M dwarfs with masses below 0.6 $M_{\odot}$. This reflects the availability of more precise observational constraints, and also greater analytic tractability in modelling higher-mass stars. Recently, however, the lower main-sequence has attracted more attention, with a series of detailed models extending past the hydrogen-burning limit to the boundary between low-mass brown dwarfs and giant planets. Understanding the structure and evolution of stars is a basic goal of stellar astronomy. Critical tests of the evolution theory for stars can be made on a small set of eclipsing binary stars (Baraffe et al. 1998; Girardi et al. 2002; Siess, Forestini, & Dougados 1997; Chabrier, Gallardo, & Baraffe 2007). While the results of stellar evolution models compare favorably to data for main-sequence stars with masses greater than that of the Sun, evidence has been growing that the models for stars on the lower main-sequence have problems when confronted with precise masses and radii from double-lined eclipsing binaries. As shown by Torres & Ribas (2002) the evolutionary models underestimate the radii and overestimate the effective temperatures of the low-mass stars. These discrepancies were confirmed in subsequent studies by Ribas (2003), Lopez-Morales & Ribas (2005), Torres et al. (2006), Morales et al. (2009a), Morales et al. (2009b), and others. Hints of the radius discrepancies have also been described by Popper (1997), Clausen, Hett, & Olsen (1999), and others. Recently, Mullan & MacDonald (2001), Torres et al. (2006), Morales, Ribas, & Jordi (2008) proposed a hypothesis based upon the effects of stellar activity to explain the discrepancies. Furthermore Stassun et al. (2009) called attention to the fact that low-mass stars appear older or younger in the mass-radius diagram depending on whether post- or pre-main-sequence models are used. As the number of low-mass eclipsing binaries studied carefully, both photometrically and spectroscopically, increases, a better comparison with the theoretical models can be made.

Light variability of NSVS 11868841 (α = $23^h17^m58^s$, $\delta = +19°17'03''$ (J2000), hereafter NSVS 1186) was detected by Wozniak et al. (2004) from data of the *Northern Sky Variability Survey*. They classified it as a detached eclipsing binary with combined median magnitude $V = 14^m.084 \pm 0.076$ and an orbital period of 0.60179 days. High-precision light curves in the Johnson V-, R-, and I-bandpass were obtained by Coughlin & Shaw (2007). Since the radial velocities of the components were not available they determined the radii of the stars by analyzing the V- and R-bandpass light curves. In this study we present the first radial velocities obtained for the components of the double-lined, short-period eclipsing binary NSVS 1186 and the physical parameters derived from the analyses of the radial velocities and the light curves. Both components show high level chromospheric activity, evidenced by Hα emission lines in their spectra. We discuss the properties of the binary and their relation to the discrepancies between empirical and theoretical mass-radius and mass-effective temperature relations for low-mass stars.

2. SPECTROSCOPIC OBSERVATIONS

2.1. *Spectroscopy*

Since wide-band light curves of NSVS 1186 are available we observed the star spectroscopically. Optical spectroscopic observations were obtained with the Turkish Faint Object Spectrograph Camera (TFOSC) attached to the 1.5 m telescope,[4] on August 23, 24, and 25, 2008 under good seeing conditions. The wavelength coverage of each spectrum was 4100–8100 Å in 11 orders, with a resolving power of $\lambda/\Delta\lambda \approx 7000$ at 6563 Å and an average signal-to-noise ratio (S/N) of ~ 150. We also obtained a high S/N spectrum of the M dwarfs GJ 740 (M0 V) and GJ 623 (M1.5 V) for use as templates in the derivation of the radial velocities (Nidever et al. 2002).

The electronic bias was removed from each image and we used the CRREJECT option for cosmic ray removal. The echelle spectra were extracted and wavelength calibrated using a Fe-Ar lamp source with help of the IRAF ECHELLE package. The stability of the instrument was checked by cross correlating the spectra of the standard star against each other using the FXCOR task in IRAF. The standard deviation of the differences between the velocities measured using FXCOR and the velocities in Nidever et al. (2002) was about 1.1 km s^{-1}.

2.1.1. *Spectral Types and Temperature Estimates*

We have used the spectra to reveal the spectral type of the primary component of NSVS 1186. For this purpose we have degraded the spectral resolution from 7000 to 3000, in order to use the calibrations by Hernández et al. (2004) by convolving the data with a Gaussian kernel of the appropriate width, and we have measured the equivalent

[4]Further details on the telescope and the spectrograph can be found at `http://www.tug.tubitak.gov.tr`.

TABLE 1

EQUIVALENT WIDTHS OF THE SELECTED LINES IN THE SPECTRA

Spectral lines	EW_p (Å)	EW_s (Å)
Ca I λ 4226	2.13±0.11	1.39±0.12
Fe I λ 5329	1.11±0.11	0.99±0.12
Fe I λ 4271	1.44±0.13	1.41±0.12
Ca I+Fe I λ 5270	2.91±0.21	2.11±0.21
Ca I λ 6162	1.99±0.42	1.11±0.09
Fe I λ 5079	0.79±0.07	0.47±0.11

widths (EW) of photospheric absorption lines for the spectral classification. We have followed the procedures described by Hernández et al. (2004), choosing metallic lines in the blue-wavelength region, where the contribution of the primary component is considerably larger than that of the secondary. From several spectra we measured equivalent widths of some spectral lines assuming the light contribution of the primary star is 0.6, as given in Table 1.

From the calibration relations of EW-Spectral-type given by Hernández et al. (2004), we have derived a spectral type of G9±1 for the primary component. The effective temperature deduced from the calibrations of Drilling & Landolt (2000), de Jager & Nieuwenhuijzen (1987) and Popper (1980) is, respectively, 5230±80, 5230±80, and 5330±141 K for the primary component. The mean effective temperature of the primary component deduced from the spectra is 5250±95 K .

NSVS 1186 is listed in several large photometric databases consolidated in the *Naval Observatory Merged Astronomical Dataset* (NOMAD-1.0, Zacharias et al. 2004), which provides optical magnitudes of $B = 14^m.77 \pm 0^m.02$, $V = 13^m.87 \pm 0^m.01$, $R = 13^m.94 \pm 0^m.01$, $I = 12^m.74 \pm 0^m.02$. Since the magnitudes collected from photographic measurements and the colors are inconsistent no attempt has been made to calculate the effective temperatures of the components. The infrared magnitudes are taken from 2MASS (Cutri et al. 2003) catalog as $J = 12^m.518 \pm 0^m.023$, $H = 12^m.069 \pm 0^m.021$, and $K = 11^m.995 \pm 0^m.019$. The observed infrared colours $J - H = 0^m.449 \pm 0^m.031$ and $H - K = 0^m.074 \pm 0^m.028$ correspond to a combined spectral type of G9±2, in a good agreement with that we derived by spectral lines alone. Using the depth of the eclipses in three bands we estimate the light contribution of the primary component as 0.60, 0.57, 0.55 and 0.56 in the V, J, H and K bands, respectively. Hence, the $V - K$, $J - H$ and $H - K$ colors of the primary component correspond to a spectral type of G9±2. We estimate a temperature of 5240±230 K from the calibrations of Tokunaga (2000). The temperature uncertainty of the primary component results from considerations of spectral type uncertainties, and calibration differences. The effective temperature of the primary star that we derived from infrared photometric measurements is in a good agreement with that we estimated from the spectra alone. The weighted mean of the effective temperature of the primary component is 5250±135 K.

2.1.2. *Rotational Velocities of the Components*

The width of the cross-correlation profile is a good tool for the measurement of $v \sin i$ (see e.g., Queloz et al. 1998). The rotational velocities ($v \sin i$) of the two components were obtained by measuring the FWHM of the CCF peaks in nine high-S/N spectra of NSVS 1186 acquired close to the quadratures, where the spectral lines have the largest Doppler-shifts. In order to construct a calibration curve FWHM-$v \sin i$, we used an average spectrum of HD 27962, acquired with the same instrumentation. Since the rotational velocity of HD 27962 is very low, but not zero ($v \sin i \simeq 11$ km s^{-1}, e.g., Royer, Zorec, & Gómez 2004, and references therein), it could be considered as a useful template for low-mass stars rotating faster than $v \sin i \simeq 10$ km s^{-1}. The spectrum of HD 27962 was synthetically broadened by convolution with rotational profiles of increasing $v \sin i$ in steps of 5 km s^{-1}, and the cross-correlation with the original one was performed at each step. The FWHM of the CCF peak was measured and the FWHM-$v \sin i$ calibration was established. The $v \sin i$ values of the two components of NSVS 1186 were derived from the FWHM of their CCF peaks and the aforementioned calibration relations, for few wavelength regions and for the best spectra. As a result, a projected rotational velocity of 77 ± 3 km s^{-1} for the primary star and of 62 ± 4 km s^{-1} for the secondary star were estimated. However, note that the spectral lines of the components could not be separated even at quadrature. Thus, the projected rotational velocities estimated in this way should involve larger uncertainties than those given here.

3. ANALYSIS

3.1. *The Orbital Configuration*

To derive the radial velocities for the components of binary system, the 16 TFOSC spectra of the eclipsing binary were cross-correlated against the spectrum of GJ 740, a single-lined M0V star,

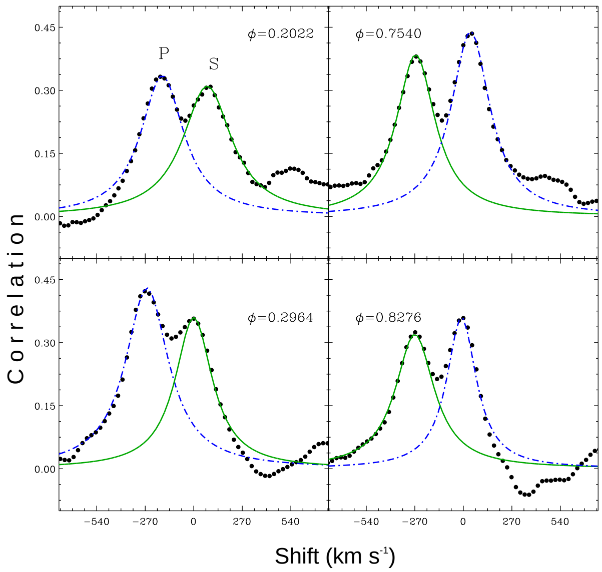

Fig. 1. Sample of cross correlation functions (CCFs) between NSVS 1186 and the radial velocity template spectrum around first and second quadrature.

on an order-by-order basis using the FXCOR package in IRAF[5]. The majority of the spectra showed two distinct cross-correlation peaks in quadrature, one for each component of the binary. Thus, to measure the velocity and errors of the individual components both peaks were fitted independently in quadrature with a Gaussian profile. If the two peaks appeared blended, a double Gaussian was applied to the combined profile using DE-BLEND function in the task. For each of the 16 observations we then determined a weighted-average radial velocity for each star from all orders without significant contamination by telluric absorption features. Here we used as weights the inverse of the variance of the radial velocity measurements in each order, as reported by FXCOR. In these data, we find no evidence for a third component, since the cross-correlation function showed only two distinct peaks. We adopted a two-Gaussian fit algorithm to resolve cross-correlation peaks near the first and second quadratures when spectral lines are visible separately. Figure 1 shows examples of cross-correlations obtained by using the largest FWHM at nearly first and second quadratures. The two peaks, non-blended, correspond to each component of NSVS 1186. The stronger peaks in each CCF correspond to the more luminous component, which has a larger weight into the observed spectrum.

[5]IRAF is distributed by the National Optical Observatory, which is operated by the Association of the Universities for Research in Astronomy, inc. (AURA) under cooperative agreement with the National Science Foundation.

TABLE 2

HELIOCENTRIC RADIAL VELOCITIES OF NSVS 1186[a]

HJD 2400000+	Phase	Star 1		Star 2	
		$V_{\rm p}$	σ	$V_{\rm s}$	σ
55069.4412*	0.0536	−120.0	14.3	...	...
55069.4855	0.1272	−162.0	9.2	...	...
55069.5284	0.1985	−193.6	4.3	80.6	4.2
55069.5727	0.2721	−198.1	3.9	85.6	6.3
55068.3810	0.2918	−183.7	3.2	80.0	8.4
55068.4258	0.3663	−171.6	3.0	47.2	8.6
55068.4707	0.4409	−128.7	13.2	...	...
55068.5134	0.5119	−68.2	14.9	...	...
55068.5578	0.5857	−28.6	11.1	...	...
55067.3674	0.6076	−6.0	7.3	−184.6	19.7
55068.6006	0.6568	19.2	3.3	−214.3	12.6
55067.4122	0.6820	28.3	3.1	−235.1	10.2
55067.4552	0.7534	40.0	1.4	−244.3	13.3
55067.4976	0.8240	19.9	9.2	−230.6	5.2
55067.5419	0.8975	1.1	2.4	...	...
55067.5846*	0.9684	−56.5	15.5	...	...

[a]The columns give the heliocentric Julian date, the orbital phase, the radial velocities of the two components and the corresponding standard deviations.

*These data were not used in the RV analysis.

The heliocentric radial velocities for the primary ($V_{\rm p}$) and the secondary ($V_{\rm s}$) components are listed in Table 2, along with the dates of observation and the corresponding orbital phases computed with the ephemerides given by Coughlin & Shaw (2007). The velocities in this table have been corrected to the heliocentric reference system by adopting a radial velocity of 9.5 km s^{-1} for the template star GJ 740. The radial velocities listed in Table 2 are the weighted averages of the values obtained from the cross-correlation of orders #4, #5, #6 and #7 of the target spectra with the corresponding order of the standard star's spectrum. A weight $W_i = 1/\sigma_i^2$ has been given to each measurement. The standard errors of the weighted means have been calculated on the basis of the errors (σ_i) of the radial velocity values for each order according to the usual formula (e.g., Topping 1972). The σ_i values are computed by FXCOR according to the fitted peak height, as described by Tonry & Davis (1979).

First we analysed the radial velocities given in Table 2 for the initial orbital parameters. We held fixed the orbital period and computed the eccentricity of the orbit, the systemic velocity and the semi-amplitudes of the radial velocities. The results of

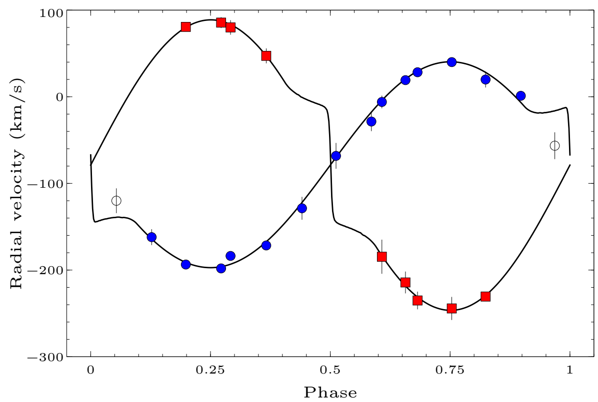

Fig. 2. Radial velocity curve folded on an orbital period of 0.601790 days, where phase zero is defined to be at primary mid-eclipse. Symbols with error bars show the RV measurements for two components of the system (primary: circles, secondary: squares). Open circles were excluded from the RV analysis.

the analysis performed with PHOEBE are as follows: $e = 0.002 \pm 0.001$, i.e. formally consistent with a circular orbit, $\gamma = -80 \pm 3$ km s^{-1}, $K_1 = 118 \pm 5$ and $K_2 = 169 \pm 6$ km s^{-1}. Using these values we estimated the projected orbital semi-major axis and the mass ratio as: $a \sin i = 3.412 \pm 0.093\ R_\odot$ and $q = M_2/M_1 = 0.70 \pm 0.04$. The observed and calculated radial velocities of both components are plotted in Figure 2 for comparison.

3.2. *Modelling the Light Curves*

As we mentioned in § 1 the V-, R- and I-bandpass light curves were obtained by Coughlin & Shaw (2007). The differential magnitudes and orbital phases were read out carefully by the method of DEXTER[6]. We used the most recent version of the eclipsing binary light curve modelling algorithm of Wilson & Devinney (1971, with updates), as implemented in the PHOEBE code of Prša & Zwitter (2005). The code needs some input parameters, which depend upon the physical structures of the component stars. In the light curve solution we fixed some parameters whose values can be estimated from global stellar properties, such as effective temperature of the primary component and mass ratio. The weighted mean of the effective temperature has been estimated to be 5250±135 K and the mass ratio 0.70±0.04. Using these values we adopted the linear limb-darkening coefficients from van Hamme (1993) as 0.39 and 0.28 for the primary and secondary components, respectively; the bolometric albedos from Lucy (1967) as 0.5, typical for a convective stellar

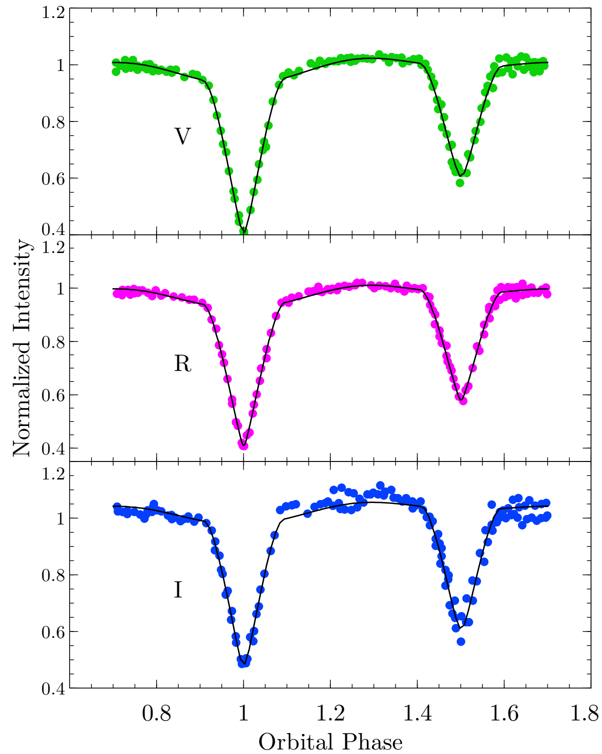

Fig. 3. The phase folded V-, R- and I-bandpass light curves for NSVS 1186. The best fitting solutions represented by the solid lines are also plotted for comparison (see text).

envelope, the gravity brightening coefficients as 0.32 for the both components. The components are assumed to be in synchronous rotation. We start with the adjustable parameters: the orbital inclination, i, the effective temperature of the less massive star, T_{eff_2}, the potential of the components, Ω_1 and Ω_2, and the monochromatic luminosity of the more massive star, L_1. Assuming it is a detached binary we used MODE-2 of the DC program for the individual solution. First we determined the preliminary elements and compared them with the observed light curves. Since the observed light curves show distortions we started with the two-spot solution, one on the primary and the other on the secondary component. The initial spot parameters were adopted from Coughlin & Shaw (2007). A best fit was obtained for each light curve using the same spots, and the corresponding parameters are given in Table 3. The parameter presented in the last column is the weighted mean of the parameters obtained from the individual light curves. The light curves along with the best-fitting solutions are shown in Figure 3.

[6] http://dc.zah.uni-heidelberg.de/sdexter.

TABLE 3

RESULTS OF THE V-, R- AND I-BANDPASS LIGHT CURVE ANALYSIS FOR NSVS 1186[a]

Parameters	V	R	I	Adopted
i°	87.0±0.5	88.6±0.2	88.3±0.2	88.0±0.4
T_{eff_1} (K)	5250[Fix]	5250[Fix]	5250[Fix]	5250[Fix]
T_{eff_2} (K)	5040±12	4990±14	5110±34	5020±16
Ω_1	4.242±0.049	4.274±0.049	4.260±0.072	4.262±0.052
Ω_2	3.810±0.026	3.739±0.020	3.989±0.054	3.790±0.026
r_1	0.289±0.004	0.288±0.004	0.286±0.006	0.288±0.004
r_2	0.263±0.003	0.267±0.002	0.250±0.005	0.264±0.003
$L_1/(L_1+L_2)$	0.604±0.009	0.586±0.009	0.591±0.013	···
$\sum(W(O-C)^2)$	0.041	0.026	0.131	···
Weight	3	5	1	···

[a]The adopted values are the weighted means of the values determined from the individual light curves.

Coughlin & Shaw (2007) analyzed only V- and R-light curves. Our analysis gives very different parameters when compared with those obtained by them. They estimate very low effective temperatures for the components with respect to their predicted masses. The fractional radii for the primary and secondary stars obtained by them are 15% and 20% smaller than those obtained by us using the same light curves. In contrast, the absolute radii are 5% and 3% larger than we found. The main difference is the location of the spots on the surface of the stars. The spot parameters given by them for the stars should be interchanged. One spot on the south pole of the primary and one spot on the north pole of the secondary represent well the three-color light curves. The spot coverage on the surface of the stars is about 8%.

3.3. *Absolute Parameters*

Combining the parameters obtained by radial velocity and light curve analyses we calculated the physical parameters of the components as listed in Table 4. We compared the locations of the components in the effective temperature-luminosity diagram, i.e., Hertzsprung-Russell diagram (Figure 4). While the location of the more massive primary star agrees well with that of a star having its mass, the secondary component appears to be more luminous, probably due to a larger effective temperature and radius. We also computed the radii of the components as $R_1 = 0.983 \pm 0.030\ R_{\odot}$ and $R_2 = 0.901 \pm 0.026\ R_{\odot}$ for the primary and secondary stars, respectively.

We computed the luminosities of the components using these radii and effective temperatures as $L_1 = 0.649 \pm 0.069\ L_{\odot}$ and $L_2 = 0.456 \pm 0.049\ L_{\odot}$ for the primary and secondary stars, respectively. We compared the positions of the components in the $L - T_e$ diagram with evolutionary tracks of pre- and post- main sequence evolution and as well as with the ZAMS, as shown in Figure 4. For constructing the solar metallicity ZAMS and evolutionary tracks, we used the Cambridge version of the the STARS code which was originally developed by Eggleton (1971) and substantially updated by Eldridge & Tout (2004). The current version is also capable of accounting for molecular contributions in the equation of state according to the Marigo (2002) approximation, which may be crucial for low mass stars. The less massive component seems to be hotter and more luminous with respect to the models. The physical parameters determined by us are very different from those obtained by Coughlin & Shaw (2007). While they estimate effective temperatures between 4370 and 5250 K from the observed colours they adopted an effective temperature of 3970 K for the more massive star. The masses of the components were estimated to be 0.94 $M_{\odot}$ and 0.87 $M_{\odot}$, the radii 1.03 $R_{\odot}$ and 0.93 $R_{\odot}$, and the effective temperature 3750 K for the secondary star. The locations of the component stars in the HR diagram correspond to stars having masses below 0.4 $M_{\odot}$. The J-,H-, and K- band extinctions in the direction of the variable were taken from Schlegel, Finkbeiner, & Davis (1998) as $A_J = 0.046$, $A_H = 0.030$ and $A_K = 0.019$ magnitudes. We computed the absolute

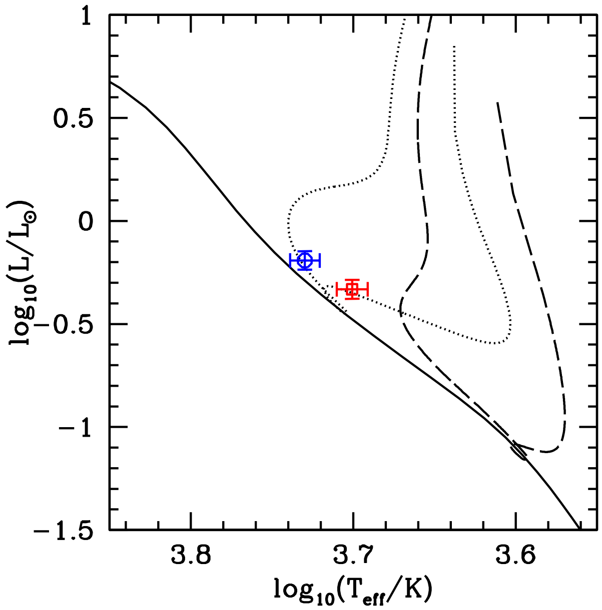

Fig. 4. Comparison between evolutionary models and the physical parameters of NSVS 1186 in the effective temperature-luminosity diagram with the luminosities determined from the light and radial velocity curves. Theoretical evolutionary tracks, both pre- and post-main sequence, for masses of 0.870 $M_{\odot}$ (dotted line) and 0.607 $M_{\odot}$ (dashed line) and ZAMS (solid line) with solar abundance were calculated with the STARS code. The circle and square denote the primary and secondary stars.

magnitudes as $M_J = 3.96 \pm 0.10$, $M_H = 3.50 \pm 0.07$ and $M_K = 3.46 \pm 0.07$ for the primary star. Then using the JHK magnitudes given in § 2.1.1 we estimate the distance to the variable as 668±25, 689±24 and 678±22 parsec in the J, H, and K bands, respectively.

4. OVERSIZED STARS IN LOW-MASS ECLIPSING BINARIES

Abt (1963) and Duquennoy, Mayor, & Halbwachs (1991) report that binary stars are more common than single stars at masses above that of the Sun. In contrast, Reid & Gizis (1997) and Delfosse et al. (1999) suggest that binaries are not very common among low-mass stars, although approximately 75% of all stars in our Galaxy are low-mass dwarfs with masses smaller than 0.7 $M_{\odot}$. Due to the low binary fractions and their faintness very few low-mass eclipsing binary systems have been observed so far both photometrically and spectroscopically, yielding accurate physical parameters. Recently, in a pioneer study, Ribas (2003, 2006) collected the available masses and radii of the low-mass stars and compared with those obtained by stellar evolution models. Despite the small numbers of the sample, a total of eight double-lined eclipsing binaries with masses and radii determined with an accuracy of better than 3%, the comparison evidently revealed that the observed radii are systematically larger than those predicted by the models. However, the effective temperatures are cooler than in the theoretical calculations, the luminosities being in agreement with those of single stars of the same mass. This discrepancy between the models and observations has been explained by Mullan & MacDonald (2001), Torres et al. (2006), Ribas (2006) and Lopez-Morales (2007) and others by the high level magnetic activity in low-mass stars. They suggest that stellar activity may be responsible for the observed discrepancy through inhibition of convection or effects of a significant spot coverage. However, Berger et al. (2006) compared the interferometric radii of low-mass stars with those estimated from theory and found a correlation between an increase in metallicity and a larger-than-expected radius, i.e. the larger radii seem to be caused by differences in metallicity.

TABLE 4

FUNDAMENTAL PARAMETERS OF THE SYSTEM

Parameter	Primary	Secondary
Mass ($M_{\odot}$)	0.870±0.074	0.607±0.053
Radius ($R_{\odot}$)	0.983±0.030	0.901±0.026
log g (cgs)	4.392±0.019	4.311±0.021
$T_{\rm eff}$ (K)	5250±135	5 020±135
log $(L/L_{\odot})$	-0.188 ± 0.045	-0.341 ± 0.046
$(v \sin i)_{\rm obs}$ (km s^{-1})	77±3	62±4
$(v \sin i)_{\rm calc}$ (km s^{-1})	83±3	76±2

The number of double-lined low-mass eclipsing binaries having precise photometric and spectroscopic observations is now 21, as far as the authors know. Combining the results of the analysis of both photometric and spectroscopic observations accurate masses, radii, effective temperatures and luminosities of the components have been obtained. In Table 5 we list absolute parameters for the low-mass stars with their standard deviations. In Figure 5 we plot the radii of the low-mass stars in eclipsing binary systems as a function of mass. Theoretical mass-radius ($M - R$) diagrams for the zero-age main-sequence stars with solar abundance taken from the STARS code and Siess, Dufour, & Forestini (2000) are also plotted for comparison.

The stars below 0.3 $M_{\odot}$ appear to trace the theoretical $M - R$ diagram. However, larger mass stars, above 0.3 $M_{\odot}$, significantly deviate from the theo-

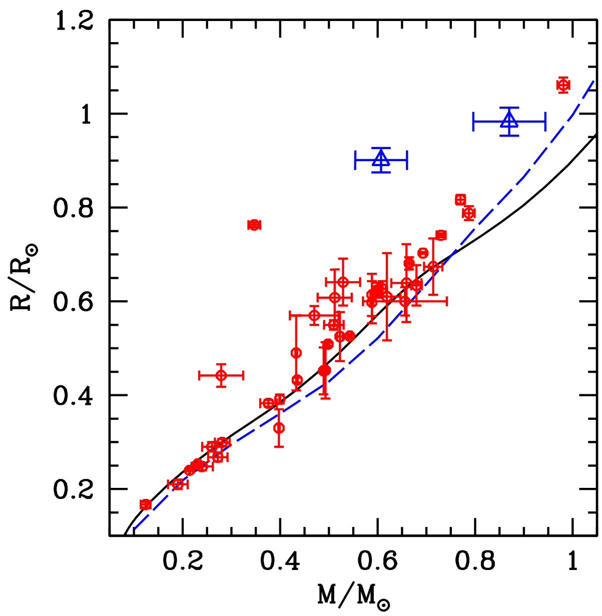

Fig. 5. Locations of the low-mass stars in the mass-radius diagram. The components of NSVS 1186 are shown by triangles. The solid and dashed lines represent the ZAMS models taken from the STARS code and Siess et al. (2000), respectively, with solar abundance.

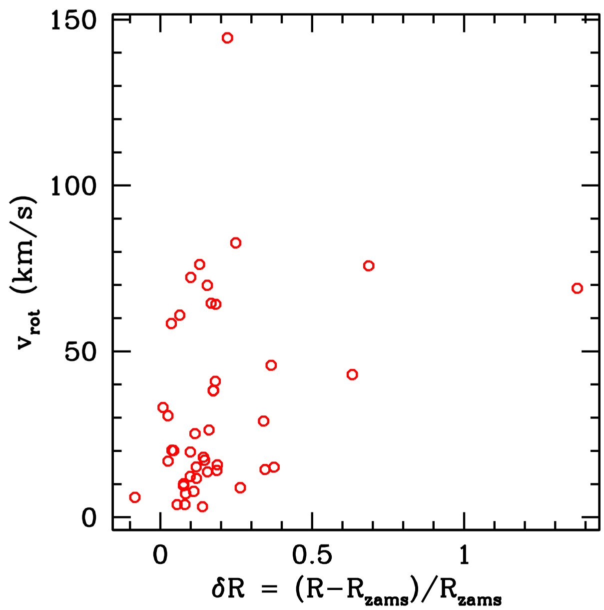

Fig. 6. The rotational velocities are plotted against the radius difference from the ZAMS at the same mass.

retical $M-R$ digram. We also computed projected rotational velocities of the components using their radii and orbital periods. Since the orbital periods are generally short, we assumed spin-orbit synchronization. The rotational velocities are plotted in Figure 6 as a function of the radius difference calculated as $(R_{\rm obs}-R_{\rm zams})/R_{\rm zams}$. This plot shows that as the rotational velocity increases, the difference in radius, gets larger for the stars given in Table 5.

A low-mass star has a convective atmosphere with a radiative core. The depth of the convective zone is about 0.28 R for a star of mass of about 0.9 $M_\odot$, and gradually increases to about 0.41 R for a star with a mass of about 0.4 $M_\odot$. Stars are thought to be fully convective below about 0.35 $M_\odot$. Therefore, the internal structure of such a low-mass star with a deep convective zone is tightly dependent on the mixing length parameter, α. In Figure 7a and b we compare locations of the low-mass stars in the $M-R$ and $M-T_{\rm eff}$ diagrams with the theoretical calculations for various α parameters. Convection is modelled by mixing length theory (Böhm-Vitense 1958) with the ratio of mixing length to pressure scale height (i.e., $\alpha = l/H_{\rm p}$). Theoretical models show that there is no significant separation in the $M-R$ relation for the stars below about 0.6 $M_\odot$, depending on the mixing length parameter. For masses above this value a separation is revealed. However, as the α parameter increases the computed effective temperature also increases. A separation is clearly seen even for the masses below 0.6 $M_\odot$. We also plotted empirical parameters for the low-mass stars in these diagrams. This comparison clearly exposes that the discrepancies in radii and effective temperatures could not be explained only by changing the α parameter as it is obvious in the $M-R$ and $M-T_{\rm eff}$ plots represented in Figure 7. On the other hand, Demory et al. (2009) showed that there is no significant correlation between metallicity and radius for the single, low-mass stars. An alternative explanation appears to be the magnetic activity responsible for the observed larger radii but cooler effective temperatures. As demonstrated by D'Antona, Ventura, & Mazzitelli (2000), Mullan & MacDonald (2001) and Chabrier et al. (2007) magnetic fields change the evolution of low-mass stars. Due to the high magnetic activity in fast-rotating dwarfs their surfaces are covered by dark spots. Spot coverage in active dwarfs yields larger radii and lower effective temperatures.

5. DISCUSSION

We obtained the radial velocity curves for the low-mass eclipsing binary NSVS 1186. We reanalysed the existing V-, R- and I-bandpass light curves. Since the light curves are distorted they are modelled assuming one spot located on each star. Then, combining the photometric and spectroscopic

TABLE 5

MASS, RADIUS, EFFECTIVE TEMPERATURE AND ORBITAL PERIOD OF THE LOW-MASS STARS IN DOUBLE-LINED ECLIPSING BINARIES

Object	Star	Mass/$M_\odot$	Radius/$R_\odot$	$T_{\rm eff}$/K	$P_{\rm orb}$/day	Refs
CM Dra	A	0.2310±0.0009	0.2534±0.0019	3130±70	1.276	1
	B	0.2141±0.0008	0.2398±0.0018	3120±70		
YY Gem	A	0.5992±0.0047	0.6194±0.0057	3820±100	0.820	2
	B	0.5992±0.0047	0.6194±0.0057	3820±100		
CU Cnc	A	0.4349±0.0012	0.4323±0.0055	3160±150	2.794	3
	B	0.3992±0.0009	0.3916±0.0094	3125±150		
GU Boo	A	0.6101±0.0064	0.6270±0.0160	3920±130	0.492	4
	B	0.5995±0.0064	0.6240±0.0160	3810±130		
TrES-Her0-07621	A	0.4930±0.0030	0.4530±0.0600	3500±···	1.137	5
	B	0.4890±0.0030	0.4520±0.0500	3395±···		
2MASS J05162881+2607387	A	0.7870±0.0120	0.7880±0.0150	4200±···	2.619	6
	B	0.7700±0.0090	0.8170±0.0100	4154±···		
UNSW-TR 2	A	0.5290±0.0350	0.6410±0.0500	···	2.144	7
	B	0.5120±0.0350	0.6080±0.0600	···		
NSVS 06507557	A	0.6560±0.0860	0.6000±0.0300	3960±80	0.520	8
	B	0.2790±0.0450	0.4420±0.0240	3365±80		
NSVS 02502726	A	0.7140±0.0190	0.6740±0.0600	4300±200	0.560	9
	B	0.3470±0.0120	0.7630±0.0050	3620±205		
T-Lyr1-17236	A	0.6795±0.0107	0.6340±0.0430	4150±···	8.430	10
	B	0.5226±0.0061	0.5250±0.0520	3700±···		
2MASS J01542930+0053266	A	0.6590±0.0310	0.6390±0.0830	3730±100	2.639	11
	B	0.6190±0.0280	0.6100±0.0930	3532±100		
GJ 3236	A	0.3760±0.0170	0.3828±0.0072	3310±110	0.770	12
	B	0.2810±0.0150	0.2992±0.0075	3240±110		
SDSS-MEB-1	A	0.2720±0.0200	0.2680±0.0090	3320±130	0.410	13
	B	0.2400±0.0220	0.2480±0.0080	3300±130		
BD -22 5866	A	0.5881±0.0029	0.6140±0.0450	···	2.211	14
	B	0.5881±0.0029	0.5980±0.0450	···		
NSVS 01031772	A	0.5428±0.0027	0.5260±0.0028	3615±72	0.368	15
	B	0.4982±0.0025	0.5088±0.0030	3513±31		
NSVS 11868841	A	0.8700±0.0740	0.9830±0.0300	5260±110	0.602	This paper
	B	0.6070±0.0530	0.9010±0.0260	5020±110		
GJ 2069A	A	0.4329±0.0018	0.4900±0.0800	···	2.771	16
	B	0.3975±0.0015	0.3300±0.0400	···		
2MASS J04463285+1901432	A	0.4700±0.0500	0.5700±0.0200	3320±150	0.630	18
	B	0.1900±0.0200	0.2100±0.0100	2910±150		
NSVS 6550671	A	0.5100±0.0200	0.5500±0.0100	3730±60	0.193	19
	B	0.2600±0.0200	0.2900±0.0100	3120±65		
IM Vir	A	0.9810±0.0120	1.0610±0.0160	5570±100	1.309	20
	B	0.6644±0.0048	0.6810±0.0130	4250±130		
RXJ0239.1	A	0.7300±0.0090	0.7410±0.0040	4645±20	2.072	21
	B	0.6930±0.0060	0.7030±0.0020	4275±15		

References: (1) Morales et al. (2009a), (2) Torres & Ribas (2002), (3) Ribas (2003), (4) López-Morales & Ribas (2005), (5) Creevey et al. (2005), (6) Bayless & Orosz (2006), (7) Young et al. (2006), (8) Çakırlı & Ibanoğlu (2010), (9) Çakırlı, Ibanoğlu, & Güngör (2009), (10) Devor et al. (2008), (11) Becker et al. (2008), (12) Irwin et al. (2009), (13) Blake et al. (2008), (14) Shkolnik et al. (2008), (15) López-Morales et al. (2006), (16) Delfosse et al. (1999), (17) Beatty et al. (2007), (18) Hebb et al. (2006), (19) Dimitrov & Kjurkchieva (2010), (20) Morales et al. (2009b), (21) López-Morales & Shaw (2007).

solutions, we derived the absolute physical parameters for both components. The standard deviations of the parameters have been determined using the JKTABSDIM code (Southworth & Clausen 2007). The less massive component appears to have a larger radius and a higher temperature than expected for its mass. On the other hand, the primary star seems to have a larger radius but the effective temperature is in agreement with that expected for its mass. We suppose that the larger radii of both components may be due to a higher activity in the system at the time that photometry is obtained. The locations of the components in the H-R diagram have been plotted and compared with theoretical models. The secondary component seems to be slightly brighter than expected for its mass.

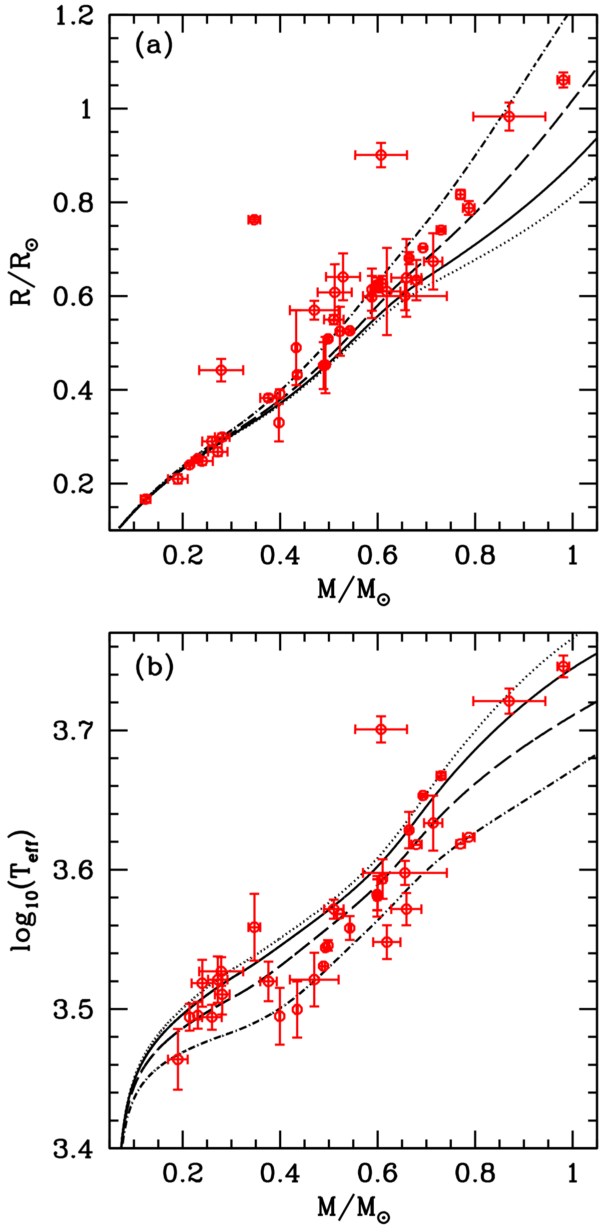

Fig. 7. Mass-radius (a) and mass-effective temperature (b) relationships for zero-age main-sequence low-mass stars calculated with the STARS code for values of the mixing length parameter $\alpha = 4$ (dotted line), $\alpha = 2$ (solid line), $\alpha = 1$ (dashed line) and $\alpha = 0.5$ (dot-dashed line). Values of the α parameter larger than 0.5 appear to affect the radius slightly for a star below 0.7 $M_{\odot}$. As α increases the effective temperatures also increase.

Basic physical parameters determined from double lined low mass binaries, such as mass, radius, effective temperature and orbital period, are collected. The locations of the low-mass stars in the mass-radius diagram are compared with the theoretical ZAMS models. Since the low-mass stars evolve very slowly, we prefer a comparison with the ZAMS models. Theoretical models tend to underestimate the radii at a given mass in the range of 0.3 and 0.6 $M_{\odot}$. Due to the evolutionary effect on the radius, we take into account only this mass range, preventing any confusion. Since low-mass stars have deeper convective layers in their atmospheres, we also computed the radii and temperatures for the abovementioned mass range for various mixing-length parameters. We find that the mixing-length parameter does not significantly affect the radii; on the contrary, it changes considerably the effective temperatures of the stars. Comparison with the observations shows that the observed larger radii of the late K and M dwarfs cannot be represented with the values of mixing-length parameters. These comparisons confirm that magnetic field induced inhibition of convection in fast-rotating low-mass stars with deep convective zones leads to larger radii and lower effective temperatures than those expected from theoretical models (D'Antona et al. 2000; Mullan & MacDonald 2001; Chabrier et al. 2007).

The authors acknowledge generous allotments of observing time at TÜBİTAK National Observatory (TUG) of Turkey. We also wish to thank the Turkish Scientific and Technical Research Council for supporting this work through grant Nr. 108T210 and EBİLTEM Ege University Science Foundation Project No:08/BİL/027. Dr. Esin Sipahi is acknowledged for the aid during the computation. We would like express our sincere gratitude to the anonymous referee, whose suggestions made the paper much clearer.

REFERENCES

Abt, H. A. 1963, ApJS, 8, 99

Baraffe, I., Chabrier, G., Allad, F., & Hauschildt, P. H. 1998, A&A, 337, 403

Bayless, A. J., & Orosz, J. A. 2006, ApJ, 651, 1155

Beatty, T. G., et al. 2007, ApJ, 663, 573

Becker, A. C., et al. 2008, MNRAS, 386, 416

Berger, D. H., et al. 2006, ApJ, 644, 475

Blake, C. H., Torres, G., Bloom, J. S., & Gaudi, B. S. 2008, ApJ, 684, 635

Böhm-Vitense, E. 1958, Zert. Astrophys., 46, 108

Chabrier, G., Gallardo, J., & Baraffe, I. 2007, A&A, 472, 17

Clausen, J. V., Helt, B. E., & Olsen, E. H. 1999, in ASP Conf. Ser. 173, Theory and Tests of Convection in Stellar Structure, ed. A. Giménez, E. F. Guinan, & B. Montesinos (San Francisco: ASP), 321

Coughlin, J. L., & Shaw, J. S. 2007, J. Southeastern Assoc. Res. Astron., 1, 7C

Creevey, O. L., et al. 2005, ApJ, 625, L127
Cutri, R. M., et al. 2003, The IRSA 2MASS All-Sky Point Source Catalog, NASA/IPAC Infrared Science Archive (Pasadena, CA: NASA/CalTech), http://irsa.ipac.caltech.edu/applications/Gator/
Çakırlı, Ö., & Ibanoğlu, C. 2010, MNRAS, 401, 1141
Çakırlı, Ö., Ibanoğlu, C., & Güngör, C. 2009, New Astron., 14, 496
D'Antona, F., Ventura, P., & Mazzitelli, I. 2000, ApJ, 543, L77
Delfosse, X., Forveille, T., Mayor, M., Burnet, M., & Perrier, C. 1999, A&A, 341, 63
de Jager, C., & Nieuwenhuijzen, H. 1987, A&A, 177, 217
Demory, B.-O., et al. 2009, A&A, 505, 205
Devor, J., et al. 2008, ApJ, 687, 1253
Dimitrov, D. P., & Kjurkchieva, D. P. 2010, MNRAS, 406, 2559
Drilling, J. S., & Landolt, A. U. 2000, in Allen's Astrophysical Quantities, ed. A. N. Cox (4th ed., New York: AIP/Springer), 381
Duquennoy, A., Mayor, M., & Halbwachs, J.-L. 1991, A&AS, 88, 281
Eggleton, P. P. 1971, MNRAS, 151, 351
Eldridge, J. J., & Tout, C. A. 2004, MNRAS, 348, 201
Girardi, L., Bressan, A., Bertelli, G., & Chiosi, C. 2002, A&AS, 141, 371
Hebb, L., Wyse, R. F. G., Gilmore, G., & Holtzman, J. 2006, AJ, 131, 555
Hernández, J., Calvet, N., Briceño, C., Hartmann, L., & Berlind, P. 2004, AJ, 127, 1682
Irwin, J., et al. 2009, ApJ, 701, 1436
López-Morales, M. 2007, ApJ, 660, 732
López-Morales, M., Orosz, J. A., Shaw, J. S., Havelka, L., Arévalo, M. J., McIntyre, T., & Lázaro, C. 2006, arXiv:astro-ph/0610225
López-Morales, M., & Ribas, I. 2005, ApJ, 631, 1120
López-Morales, M., & Shaw, J. S. 2007, in ASP Conf. Ser. 362, The Seventh Pacific Rim Conference on Stellar Astrophysics, ed. Y. W. Kang, H.-W. Lee, K.-C. Leung, & K.-S. Cheng (San Francisco: ASP), 26
Lucy, L. B. 1967, Zert. Astrophys., 65, 89
Marigo, P. 2002, A&A, 387, 507
Morales, J. C., Ribas, I., & Jordi, C. 2008, A&A, 478, 507
Morales, J. C., Torres, G., Marschall, L. A., & Brehm, W. 2009b, ApJ, 707, 671
Morales, J. C., et al. 2009a, ApJ, 691, 1400
Mullan, D. J., & MacDonald, J. 2001, ApJ, 559, 353
Nidever, D. L., Marcy, G. W., Butler, R. P., Fischer, D. A., & Vogt, S. S. 2002, ApJS, 141, 503
Popper, D. M. 1980, ARA&A, 18, 115
________. 1997, AJ, 114, 1195
Prša, A., & Zwitter, T. 2005, ApJ 628, 426
Queloz, D., Allain, S., Mermilliod, J.-C., Bouvier, J., & Mayor, M. 1998, A&A, 335, 183
Reid, I. N., & Gizis, J. E. 1997, AJ, 114, 1992
Ribas, I. 2003, A&A, 398, 239
________. 2006, Ap&SS, 304, 89
Royer, F., Zorec, J., & Gómez, A. 2004, in IAU Symp. 224, The A-Star Puzzle, ed. J. Zverko, J. Ziznovsky, S. J. Adelman, & W. W. Weiss (Cambridge: Cambridge Univ. Press), 109
Schlegel, D. J., Finkbeiner, D. P., & Davis, M. 1998, ApJ, 500, 525
Shkolnik, E., Liu, M. C., Reid, I. N., Hebb, L., Cameron, A. C., Torres, C. A., & Wilson, D. M. 2008, ApJ, 682, 1248
Siess, L., Dufour, E., & Forestini, M. 2000, A&A, 358, 593
Siess, L., Forestini, M., & Dougados, C. 1997, A&A, 324, 556
Southworth, J., & Clausen, J. V. 2007, A&A, 461, 1077
Stassun, K. G., Hebb, L., López-Morales, M., & Prša, A. 2009, arXiv:0902.2548
Tokunaga, A. T. 2000, in Allen's Astrophysical Quantities, ed. A. N. Cox (4th ed. New York: Springer), 143
Tonry, J., & Davis, M. 1979, AJ, 84, 1511
Topping, J. 1972, Errors of Observation & Their Treatment (London: Chapman & Hall Ltd.)
Torres, G., Lacy, C. H., Marschall, L. A., Sheets, H. A., & Mader, J. A. 2006, ApJ, 640, 1018
Torres, G., & Ribas, I. 2002, ApJ, 567, 1140
van Hamme, W. 1993, AJ, 106, 2096
Wilson, R. E., & Devinney, E. J. 1971, ApJ, 166, 605
Wozniak, P. R., et al. 2004, AJ, 127, 2436
Young, T. B., Hidas, M. G., Webb, J. K., Ashley, M. C. B., Christiansen, J. L., Derekas, A., & Nutto, C. 2006, MNRAS, 370, 1529
Zacharias, N., Monet, D. G., Levine, S. E., Urban, S. E., Gaume, R., & Wycoff, G. L. 2004, BAAS, 36, 1418

Ö. Çakırlı, C. İbanoğlu, and A. Dervişoğlu: Ege University, Science Faculty, Astronomy and Space Sciences Dept., 35100 Bornova, İzmir, Turkey (omur.cakirli@ege.edu.tr).